UCRL- 90871
PREPRINT

ENERGY DEPENDENCE OF NEUTRON SCATTERING FROM ^{208}Pb IN THE ENERGY RANGE 7-50 MeV

R. W. Finlay, J.R.M. Annand, T. S. Cheema
and J. Rapaport
Ohio University, Athens, Ohio 45701

and

F. S. Dietrich
Lawrence Livermore National Laboratory
Livermore, California 94550

This paper was prepared for submittal to
Physical Review C

May 1984

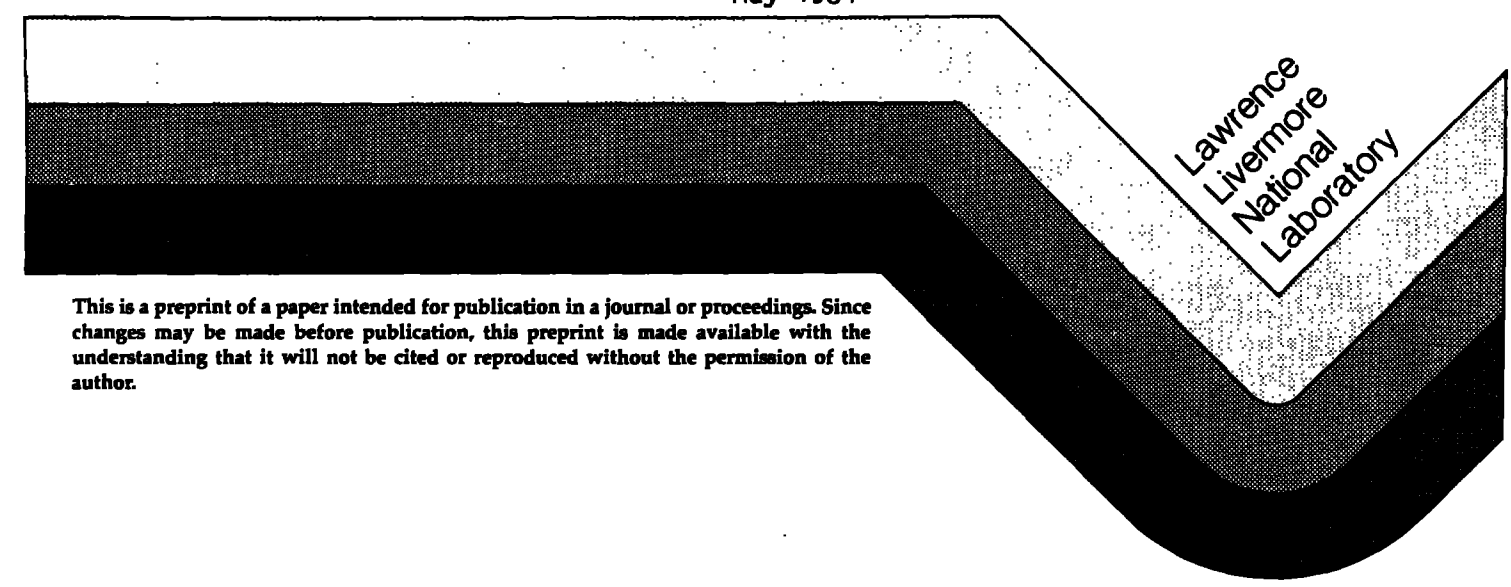

ENERGY DEPENDENCE OF NEUTRON SCATTERING FROM ^{208}Pb IN THE ENERGY RANGE 7-50 MeV

R.W. Finlay, J.R.M. Annand, T.S. Cheema[†], J. Rapaport

Ohio University, Athens, Ohio 45701

and

F.S. Dietrich

Lawrence Livermore National Laboratory

Livermore, California 94550

Elastic neutron scattering from ^{208}Pb has been measured at 22.0 and 24.0 MeV and remeasured at 7.0 and 20.0 MeV with greatly improved precision. The present results and other neutron data in the energy range 7-50 MeV are analyzed in terms of a conventional, local optical model potential with the aim of studying energy dependence of the potential well depths. We find that the very detailed measurements of the present work make unusual demands on the geometrical parameters of the model. Improvements, if any, resulting from extension of the optical model parameterization to include a real surface term and imaginary spin-orbit term are tested. Concurrently with the elastic scattering experiments, inelastic scattering to the 3^- state at 2.615 MeV was measured at 7.0, 20.0 and 22.0 MeV. A DWBA analysis is made of these data to extract octupole deformation parameters.

---

† Permanent address: Punjab University, Chandigarh, India.

NUCLEAR REACTIONS ^{208}Pb(n,n), E = 7.0, 20.0, 22.0, 24.0 MeV; ^{208}Pb(n,n'), En = 7.0, 20.0, 22.0 MeV; measured $\sigma(E,\theta)$, deduced optical model and octupole deformation parameters.

1. Introduction

The description of elastic scattering of nucleons from nuclei in terms of a local optical model has enjoyed considerable success for many years. Although the phenomenological model contains a large number of parameters, experience has shown that scattering data over a wide range of target nuclei and incident nucleon energy can be described in terms of global[1,2] potentials in which the parameters show a smooth and sensible variation with projectile energy and with the neutron and proton number of the target nucleus.

A typical phenomenological optical model study might begin with the measurement of differential elastic nucleon scattering from a given target nucleus over a wide range of projectile energy. Best fits to the cross sections are obtained by variation of the parameters of the optical model potential. In order to study the energy dependence of the potential well depths, a single set of geometrical parameters is frequently chosen by averaging the results of the individual best fits and the data are fit again with automatic search codes which vary only the well depths until the best description of the data is obtained.

An example of a typical optical model study, and an important antecedent for the present work, is the earlier study of neutron scattering from ^{208}Pb by Rapaport et al.[3] and by Cheema,[4] in which elastic scattering differential cross sections were measured at 7, 9, 11, 20 and 25.7 MeV. Inelastic

scattering to the 3^- state at 2.615 MeV was also measured at 11 and 25.7 MeV.[5] In the analysis of ref. [3] reasonable fits to the elastic scattering data were obtained with three different requirements for the geometrical parameters: a) a free-parameter search, b) a fixed, average geometry, and c) a fixed geometry with the parameters used by Van Oers et al.[6] in a study of 15-1000 MeV proton elastic scattering from Pb. This third parameterization facilitated the comparison with proton scattering and provided information on the Coulomb correction term and the symmetry term in the nucleon-nucleus optical potential model.

A combination of recent work and careful comparison with earlier work caused us to question the accuracy of some of our earlier measurements[3,4] and provided the motivation for the extensive new measurements reported herein. Specifically, the present measurements at 7.0 MeV and 20.0 MeV are intended to replace the measurements reported at 7.0 MeV and 20.0 MeV in ref. [3,4]. While the precision of the new data provides ample justification for this replacement, some discussion of the original thinking that led to the remeasurements is warranted.

At 7.0 MeV the cross sections of ref. [3,4] are larger than the unpublished values of Kinney and Perey[7] at small angles ($\theta \lesssim 25$). Measurements in ref. [7] extend to smaller scattering angles than those of ref. [3] and are actually in good agreement with the systematic optical model analysis of ref. [3]. On the other hand, the data of Kinney and Perey do not extend as far in the backward direction. A third measurement at 7.5 MeV[8] does not clarify the situation because of insufficient detail at the small angles. Thus, it was decided to remeasure ^{208}Pb(n,n) at 7.0 MeV in as much detail as was possible using current, improved techniques.

At 20.0 MeV there were no other data with which to compare the work of refs. [3,4]. Although the forward angles were also difficult to fit for these data and they are less detailed than the measurement at 25.7 MeV[3,5], they were not seriously questioned until the beam swinger measurements of DeVito et al.[9] were analyzed by DeLeo and Micheletti[10]. From the systematics presented in refs. [9-10] it seemed likely that the imaginary potential depth required to fit the data at 20.0 MeV was unrealistically large. On the basis of these considerations, ^{208}Pb (n,n) was remeasured at 20.0 MeV with improved precision and detail and new measurements were added at 22.0 and 24.0 MeV.

An equally important motivation for the present work was a desire to have as complete a data set as possible for at least one spherical nucleus so that a basis would exist to test recently developed microscopic optical potential models[11,12] of nucleon-nucleus scattering. Such a test has been performed and is reported elsewhere[13]. The present work reports the impact of these improved data on the parameterization of the macroscopic, phenomenological potential.

2. Experimental Techniques

The neutron scattering measurements described in this work were made at the Ohio University Tandem Van de Graaff accelerator laboratory with the newly installed Beam Swinger time-of-flight spectrometer. This is the same beam swinger magnet that was used by DeVito (et al.[9]) for their neutron scattering measurements at 30 and 40 MeV. The original installation at Michigan State University was described by Bhowmik et al.[14], and a detailed

description of its application to neutron scattering at $E_n < 26$ MeV at Ohio is given by Finlay et al.[15)]

Monoenergetic 7.0 MeV neutrons were produced with the $^2H(d,n)^3He$ reaction. A 4.39 MeV deuteron beam was pulsed and bunched into subnanosecond bursts at 2.5 or 5 MHz repetition rate and focussed through the beam swinger magnet to a 3 cm long deuterium gas cell that was maintained at $\sim$ 2 atm pressure by a 3 μm thick W entrance foil. The $^3H(d,n)^4He$ reaction was used to produce 20, 22 and 24 MeV neutrons in gas cells of similar design. In those cases the incident deuteron energies were 3.90, 5.47 and 7.07 MeV respectively, and 5 μm thick entrance foils of either Mo or W were used. With tritium in the gas cell the pressure was never higher than 1.7 atm.

The scattering sample was a 2.0 cm diam by 3.05 cm long right circular cylinder of lead weighing 106.3 g and enriched to 98.7% in the isotope ^{208}Pb. It was mounted in an automatic sample changer at a distance of $\sim$ 14 cm from the target gas cell.

Neutrons were detected in an array of seven 2.85 ℓ NE213 liquid scintillation detectors coupled to RCA-4522 photomultiplier tubes. The flight path from the scattering sample to the neutron detector array was 12-13 m in all experiments. The technique of n-γ pulse shape discrimination was used to reject gamma ray events in the neutron detectors. Pulse height, pulse shape and time-of-flight information were stored separately for each detector and as a summed spectrum for the entire array in the OU-8000 minicomputer.[16)] A typical time-of-flight spectrum obtained at 22.0 MeV is shown in Fig. 1. Overall energy resolution was about 250 keV at 7.0 MeV and 400-450 keV at 20-24 MeV which was more than adequate in view of the well-separated energy levels in ^{208}Pb.

Neutron flux from the gas cell was monitored by a time-of-flight detector located 1 m from the neutron production target. It consisted of a 2.5 cm diam x 1 cm thick stilbene scintillator coupled to an RCA 8575 photomultiplier, rigidly attached to the beam swinger magnet so that a constant monitor flight path and angle were maintained as the swinger magnet was rotated. Individual measurements were normalized to the counting rate in the monitor, and absolute cross sections were obtained by rotating the beam swinger to zero degrees and measuring the flux in the main detector array per monitor count, with the scattering sample removed. The energy dependence of the detector relative efficiency was determined in separate measurements of the known yield of the $^{2}H(d,n)$ and $^{3}H(d,n)$ source reactions as a function of incident deuteron energy and emission angle.

3. Data Reduction and Corrections

Since one of the purposes of these experiments was to repeat earlier measurements that were in question, some unusual data-taking procedures were adopted. At 7.0 MeV, time-of-flight spectra were taken in 2.5° or 5° steps from $10° < \theta < 159.8°$. Measurements were repeated frequently at several angles as a test of the reproducibility of the results. The final results consisted of cross sections at 41 angles. The experiments of ref. [4,7,8] contained 19-29 points, which should be adequate to characterize a function that is very well represented by 13 Legendre coefficients, provided that the data points extend over a wide enough angular range. Thus, although the distribution at 7.0 MeV is somewhat overdetermined, data rates were high, and the swinger is very well suited to frequent, small changes in angle.

The location and shape of each angular minimum are well determined and should provide a stringent test for an optical model potential.

At 20-24 MeV, it is essential to measure the elastic scattering cross section at many angles in order to characterize the sharply diffracted angular distributions. For comparison with optical model calculations, the density of data points at 20-24 MeV is adequate but not excessive.

At each scattering angle, a monitor-normalized, background-subtracted time-of-flight spectrum was obtained. Neutron yields for elastic and inelastic scattering were extracted by simple channel summation programs which, due to the wide spacing of states, proved entirely adequate at all angles. The yields are corrected for detector efficiency and dead time. A small (< 2%) correction is made for the source reaction anisotropy since the source reaction cross section, averaged over the solid angle subtended by the detector, is slightly larger than the source cross section, averaged over the solid angle subtended by the scattering sample.

The data are further corrected for multiple scattering, finite geometry and neutron flux attenuation in the sample with a modified version of the Monte Carlo computer code MULCAT.[17] The convergence properties of this code have been carefully tested with large calculations using the CRAY-1 computer at Lawrence Livermore National Laboratory.

Results of the present work are discussed in Sections 5 and 6. The new experiments differ from the earlier work at 7.0 and 20.0 MeV as follows: At 7.0 MeV the new measurements are substantially lower than the old 7.0 MeV data in the forward direction ($\theta \lesssim 25$). Beyond 60°, the two sets are similar but the earlier work did not extend to the deep minimum at

155°. At 20.0 MeV, the two experiments give comparable results for $\theta < 30°$ but the new data fall off with increasing angle much more slowly than the old. The new data also locate two diffraction minima and one maximum that were not apparent because of the coarse angular steps in the old data.

The error bars on the data points in present work represent uncertainties due to normalization, counting statistics, dead time corrections, and the uncertainties associated with the Monte Carlo calculations of the multiple scattering corrections. Uncertainties from counting statistics were generally less than 2% for the 7.0 MeV data, but for the higher energy data they ranged from 1% in the forward direction to 10% at larger scattering angles; Normalization uncertainties ($\pm$ 2%) result largely from fluctuations in the yield-to-monitor ratio at zero degrees.

While the experiments were conducted primarily to study elastic scattering, some information on inelastic scattering to the 3^- state at 2.615 MeV was obtained at 7.0, 20.0 and 22.0 MeV. The results are discussed in Sec. 6.

Contributions to the elastic scattering cross section from the compound nucleus reaction mechanism were evaluated with the computer code OPSTAT[18] which performs a Hauser-Feshbach calculation with a width fluctuation correction taken from a recent prescription due to Moldauer.[19] The calculated contribution was of the order of 4% of the cross section at the 155° minimum of the 7.0 MeV angular distribution. It was entirely negligible at all other angles and energies and was neglected throughout this work. Justification of the neglect of compound elastic scattering is obtained from a separate study of elastic scattering from ^{208}Pb and ^{209}Bi

at 4.0, 4.5, 5.0, 5.5 and 6.0 MeV.[20] The parameterizations of the nuclear level density and optical potential used in the Hauser-Feshbach 7 MeV calculation were found to give reliable predictions of the lower energy cross sections, where the importance of the compound component rapidly increases.

4. Total Elastic and Reaction Cross Sections

The final, corrected elastic scattering data may be conveniently described with an expansion in Legendre polynomials. This representation provides a model-independent basis for obtaining the integrated elastic scattering cross section and for extrapolating the angular distribution beyond the range of the measurements. If the expansion can be performed with sufficient precision, a value of the reaction cross section is also obtained since

$$\sigma_{reaction} = \sigma_{total} - \sigma_{elastic}$$

and the total cross section is well known at these energies.

Let

$$\frac{d\sigma(\theta)}{d\Omega} = \sum_{L=0}^{L_{max}} a_L P_L (\cos \theta_{cm});$$

then $\sigma_{elastic} = 4\pi a_0$ and $\frac{d\sigma}{d\Omega}(0°) = \sum_L a_L$.

The values of the a_L's and the goodness of fit depend on the number of terms retained in the expansion. In principle, L_{max} should increase with increasing energy approximately as kR where k is the wave number of the incident neutron and R is the nuclear radius. In practice, the selection of L_{max} is quite unambiguous as long as the input data are sufficiently precise and cover a wide enough angular range.

In Fig. 2 we plot χ^2/N (where N = number of degrees of freedom), integrated elastic cross section and differential elastic cross section at $\theta = 0°$ all as a function of L_{max} for the differential cross section measurements at 22 MeV. It is clear that χ^2/N decreases rapidly with increasing L_{max} until $L_{max} = 20$ after which no further decrease is achieved. The values of $\sigma_{elastic}$ and $\frac{d\sigma}{d\Omega}$ (0°) are very stable for $L_{max} > 20$ but the uncertainty in the value of the forward angle cross section increases as superfluous terms are included in the expansion. For these data the optimum value of L_{max} is chosen to be 20.

Values of L_{max}, $\frac{d\sigma}{d\Omega}$ (0°), $\sigma_{elastic}$ and $\sigma_{reaction}$ obtained from Legendre fitting of the present data are given in Table 1. The accuracy of the reaction cross section obtained in this manner is slightly worse (6% vs 4%) than the values obtained from experiments specifically designed for that purpose since the present results are obtained by subtraction of well-known but large numbers.

Also shown in Table 1 are measured values of the total cross section[21,22] and the resulting values of Wick's limit.[23] The extrapolated values of $d\sigma/d\Omega$ (0°) obtained from the Legendre polynomial expansion clearly satisfy Wick's Limit at all of the energies reported here. Since the normalization uncertainties are believed to be very low ($\lesssim$ 2%) for the present measurements, the question rises as to how useful a guide Wick's limit is expected to be in assessing the accuracy of the experiment. An optical model calculation using a potential close to that of ref. [3] showed that $d\sigma/d\Omega$ (0°) is equal to Wick's limit at 7.0 and 22.0 MeV, and that the deviation from Wick's limit is less than 1% in the ranges 4.5-9.5 and 18-28 MeV. These results were found to be independent of small variations in the optical

model parameters. The near agreement ($\lesssim$ 2% difference) between the experimental values $d\sigma/d\Omega$ and Wick's limit lends strong circumstantial support for the accuracy of the normalization in the present experiment.

5. Optical Model Analysis

A local, spherical optical model potential was used in the analysis of the neutron scattering data. It consisted of a real term and an imaginary term:

$$-U(E,r) = V(E,r) + iW(E,r)$$

where

$$V(E,r) = V_R(E)\, f(X_R) - V_{S.O.}(\vec{\sigma}\cdot\vec{\ell})\left(\frac{h}{m_\pi c}\right)^2 \frac{1}{r}\frac{d}{dr} f(X_{S.O.}),$$

$$W(E,r) = W_V(E)\, f(X_I) - 4a_i W_D(E)\frac{d}{dr} f(X_I),$$

and

$$f(X_i) = (1 + \exp(X_i))^{-1},\quad X_i = (r - r_i A^{1/3})/a_i .$$

5.1 Independent Searches at Each Energy

The automatic search code OPSTAT[18] was used to obtain optimum fits to the data at each energy by variation of the potential well depths and geometrical parameters of the optical potential. The complete neutron data set included

a) new differential cross section measurements at 7.0, 20.0, 22.0 and 24.0 MeV;

b) earlier differential cross section measurements by Rapaport et al.[3] at 9.0, 11.0 and 25.7 MeV and by DeVito et al. at 30.3 and 40 MeV[9];

c) analyzing power measurements on natural lead at 7.75 MeV by Bulski et al.[24] and on ^{208}Pb at 10.0 MeV by the TUNL group[25]; and

d) total cross section measurements by Lisowski et al.[21] or by Foster and Glasgow[22] at each of these energies.

Starting values for the searches were taken from Set A of the global optical parameters of Rapaport, Kulkarni and Finlay (RKF)[1] which contains an energy independent, real spin-orbit potential the parameters of which were held constant at the values suggested by Becchetti and Greenlees.[2] For $E_n \leq 11$ MeV the imaginary potential was taken to have a derivative Woods-Saxon form. A six-parameter search (V_R, r_R, a_R, W_D, r_I, a_I) was conducted at each energy with due regard for well-known ambiguities in the parameterization of the optical model. For $E_n \geq 20$ MeV, a combination of surface and volume absorption was allowed thus introducing a seventh parameter (W_V). The parameters obtained from these individual searches are given in Table 2.

Inspection of Table 2 reveals a definite tendency, especially in the new data, for the real radius parameter to decrease with increasing energy. The sensitivity of the fits to the data at 7.0 MeV and 22.0 MeV is illustrated in Fig. 3. The solid lines represent the best fits to these angular distributions obtained by using the 22.0 MeV geometry of Table 2 and varying the well depths. The dashed lines show the best fits obtained with the 7.0 MeV geometry. The deterioration of the fit to either data set when the wrong geometry is used is clear. It would seem that, given a well determined angular distribution, the often quoted $V_R r_R^2$ and $W_D a_I$ potential parameter ambiguities, become less ambiguous after all. For each of the energies shown in Fig. 3 we have two optical model calculations

that differ in $V_R R_R^2$ and $W_D a_I$ by 3-4% but give strikingly different qualitative fits to the data as shown in the figure and as reflected by large differences in χ^2/N. The older, less well defined angular distributions can tolerate a substantially larger range of values for the geometrical parameters before the best fits would be deemed unsatisfactory.

Two other features of Table 2 deserve comment. First, the very small value of the imaginary diffuseness (a_I = .406) at 7.0 MeV appears to be anomalous but is absolutely required by our searches if the optical model calculation is to describe the deep diffraction minima, particularly that at 155 degrees. This deep minimum is an important feature of the new data. This characteristic structure was observed in the pioneering studies of n+^{206}Pb at 7.0 MeV by Zafiratos et al.[26] and was also observed in recent measurements[20] on ^{209}Bi and ^{208}Pb at 6.5 and 6.0 MeV, although for ^{208}Pb at 6.0 MeV compound elastic scattering begins to fill in the valleys.

Second, fits to the analyzing power at 7.75 and 10.0 MeV are reasonable although not quite as good as was obtained with a complex spin-orbit potential in ref. [25] at 10.0 MeV. An attempt was made to use these parameters to fit the elastic scattering cross section data at higher energies with results less satifactory than those obtained with the Becchetti-Greenlees spin orbit parameters.

5.2 Common Geometry Optical Model Calculations

In order to study the energy dependence of the optical model potential depths, it is common practice to assign fixed values to the six geometrical parameters of the model. These values can be assigned either

by averaging the values listed in Table 2 or by searching for the geometry that provides the best overall fit to the data. The second approach was adopted in the present work. Starting with parameters taken from Set A of the RFK global potential, the entire data set of Section 5.1 was fit simultaneously with geometrical parameters, as well as potential well depths, being allowed to vary. However, the geometrical parameters were constrained to be energy independent and the well depths were constrained to have piecewise linear energy dependence. The linear coefficients were varied in the search routine. Additionally the spin orbit geometry and well depth were searched. We felt justified in doing this as two analyzing power data sets are included and the latest differential cross sections are well defined at backward angles. The data set for these calculations was expanded from that quoted in Sec. 5.1 to include total cross sections in the energy gaps between the differential cross sections and analyzing powers and also in the energy range 40-50 MeV. Total cross sections were preferentially weighted in the least squares parameter search to force the fit to follow their measured energy dependence. The potential parameters resulting from this procedure are given in Table 3.

With the geometrical parameters fixed at these values, potential well depths were searched in order to obtain the best fit to the differential cross section, analyzing power and total cross section data. Resulting values of the potential well depth parameters are shown as points in Fig. 4. The lines on Fig. 4 are not a linear least squares fit to the points but are the final values of an analytical expression, given in Table 3, which provides a good description to the data everywhere in this energy region.

Fits to the differential scattering cross sections, analyzing powers and the total cross sections obtained with the analytical expression are shown in Figs. 5, 6 and 7, respectively. It is clear from these figures that a very good overall description of the data is obtained from this representation.

The optical model parameters of Table 3 do not succeed in fitting the 7.0 MeV differential cross section data beyond $\theta = 100°$ as well as the free-geometry individual best fit calculation (compare Figs. 3 and 5). It seems possible to fit the detailed shape of the cross section in this region only by increasing the real radius to $r_R \simeq 1.25$ fm and decreasing the imaginary diffuseness to $a_I \simeq 0.40$. These values would also provide a somewhat better fit to the analyzing power at 7.75 MeV but would give quite poor results at higher energy.

Better low energy fits with a real radius parameter of ~ 1.20 fm may be obtained if a weak ($\sim$ 1 MeV potential depth) derivative Woods-Saxon component, having the same geometry as the imaginary potential, is added to the real potential. The presence of such a term is predicted by Ahmad and Haider[27] on the basis of a dispersion relation between the real and imaginary parts of the optical potential, a consequence of the energy dependence of the nucleon optical potential. The inclusion of a surface peaked imaginary term in the phenomenological potential implies that a real surface peaked term should also be included. A common geometry search similar to that described above, but including a real surface potential term was attempted. The resulting potential parameters are given in Table 4. The real surface well depth was given the energy dependence predicted in Ref. [27] and an overall multiplicative term was searched

adding one degree of freedom to the calculation. The search produced a well depth about 0.24 of that predicted by Ahmad and Haider[27] with a small improvement in overall quality of fit. However, at low energy, where the magnitude of the real surface term is predicted to be a maximum, only the 7 MeV data is really sensitive to its inclusion, so that the test is far from conclusive. The matter will be addressed in a future publication.[20]

A comparison of the potential model of Table 3 with our earlier study[3] of ^{208}Pb reveals some significant differences. For example, the energy dependence of the surface absorption term still has a triangular shape (see Fig. 3 of Ref. 3); however, the peak of the triangle is somewhat blunted compared with the earlier work and the decrease of W_D with increasing energy is considerably slower. These changes stem from the inclusion of total cross section data, the data at 30 and 40 MeV of DeVito[9] and from the remeasurement, in the present work, of elastic scattering at 20 MeV. Volume integrals of the analytic model are compared with those of the Brieva-Rook microscopic model in Fig. 8. The solid lines correspond to the analytic expression of the present work while the points are the values of J/A computed from the Brieva-Rook interaction at the energies studied in Ref. [13]. The energy dependence of the phenomenological potentials follows closely the predictions of the microscopic model although we note a slight difference in the variation of J_V/A with energy. The general trend of J_W/A is much smoother than tht shown by DeLeo and Micheletti primarily because of the revised results of 20 MeV.

While the spin-orbit potential in the present model is still real and energy independent, the well depth and shape differ somewhat from the Becchetti-Greenlees values[2] used earlier.[1,3] The volume integral of the

spin-orbit potential in Table 3 is about 2% larger than the Becchetti-Greenlees value but is still about 12% smaller than the value used by Van Oers et al.[6] in their study of proton scattering from ^{208}Pb over a wide range of energies. These changes improve the fits to the entire data set and were particularly useful in fitting the troublesome large-angle elastic scattering data at 7.0 MeV. A real, energy independent spin orbit potential was the simplest prescription that gave a good description to the present data set. Including a small $\sim$ 0.5 MeV imaginary spin orbit component to the potential models of Tables 3 and 4 gave a small improvement in fit to the two analyzing power data sets. Effects on cross sections were negligible. A detailed study of neutron analyzing power over a wide range of energies would probably shed more light on the true nature of this interaction.

6. Inelastic Scattering

The latest experiments at 7.0, 20.0, 22.0 and 24.0 MeV were undertaken primarily to measure elastic scattering cross sections. However, inelastic scattering data were also extracted for the 3^- state at 2.615 MeV excitation at energies 7.0, 20.0 and 22.0 MeV and are presented in Fig. 9. In addition to the sources of error quoted for elastic cross sections, there was a contribution of about 2% from uncertainty in the energy dependence of the measured detection efficiency. The major source of error was, however, the statistical uncertainty in counting rate.

A macroscopic DWBA analysis was made of these data using the code DWUCK4[28], with distorted waves calculated using the potential model of

Table 3. At 7.0 MeV an approximately isotropic compound inelastic cross section of $\sim$ 1 mb/sr is estimated from Hauser-Feshbach model calculations. This contribution was added to the DWUCK4 output before comparing with the data. The extracted octupole deformation parameters listed in Table 5 are consistent with previous neutron[3,5] and proton[30,31] inelastic scattering analyses. Detailed comparison of the deformation lengths obtained from the present work with the results of earlier analyses (see, for example, Table 2 of Ref. 3) does not exclude the possibility of a weak isovector effect. The results also suggest a weak tendency for the deformation lengths to decrease with increasing energy. However, both of these effects are about the same size as the stated uncertainties.

Coupled channels calculations were also made at 7.0 MeV with the code ECIS79.[29] For these the first 3^- and 5^- states were coupled to the ground state in a harmonic oscillator framework. As with the DWBA analysis, the potential model of Sec. 5 was used. Taking a 5^- deformation parameter of 0.065[5] and searching the 3^- deformation parameter, yielded almost the same value as the DWBA analysis. Coupled channels effects on elastic scattering were also found to be small, and this analysis was not pursued to higher energies.

DWBA fits to the 3^- angular distributions are shown in fig. 9. While the fit is uniformly good over the full 10°-160° angular range at 7.0 MeV, it grossly underpredicts cross sections forward of 20° at 20.0 and 22.0 MeV. This feature has become apparent in the present data due to the much improved ability of the beam swinger facility to measure forward angle cross sections. It is not shown in the 25.7 Mev data of Ref. [5] where reliable measurement of the 3^- cross section was not possible forward of

20°. Neither is it apparent in proton inelastic scattering measurements at 30 and 35 MeV[30,31] which are also less well defined at forward angles. However, a similar effect can be seen in inelastic scattering from the first 2^+ state of ^{54}Fe, measured at 26.0 MeV by Mellema et al.,[32] where DWBA systematically underpredicts in the 10°-20° angular range. It is worth emphasizing at this point that the large forward angle cross sections do not result from elastic contamination. The 3^- time-of-flight peaks even at 10° are well defined with good peak to background ratio.

A qualitative theoretical explanation has been advanced[33] that this forward angle anomaly may be a manifestation of direct knock on effects. A quantitative explanation is, however, beyond the scope of this paper.

7. Conclusion

The recently measured cross sections, reported in this paper, have proved a valuable addition to the data set used in determining a phenomenological optical model of neutron scattering from ^{208}Pb. These data, which have improved precision and angular definition, demonstrate the power of a beam swinger facility for making neutron cross section measurements, and place stringent constraints on the parameterization of the model. Specifically, the increased detail serves to reduce the range of ambiguity in $V_R r_R^2$ and $W_D a_I$. Moreover, the methods of calculation adopted for the present work, which included simultaneous searches of many parameters in a very large data base, proved to be quite effective in defining the common-geometry potential model.

It has been possible to obtain an excellent description of the entire data set in terms of a conventional optical model with constant geometry, a

real, energy-independent spin-orbit potential and energy dependent real and imaginary well depths even though the individual best fits suggested the need for energy dependent geometrical parameters, particularly at 7.0 MeV. The unusual geometry required for optimum fitting of the new backward angle 7.0 MeV data may be partially explained as an inadequacy of the conventional optical model parameterization. A slight improvement in the overall fit is obtained if a surface real term, having the same geometry as the imaginary potential, is included. The importance of this term seems to be greatest at the lowest energies considered in the present work.

Regarding inelastic scattering, the present potential model has been used in a DWBA analysis of those cross sections for the first 3^- state, which were measured concurrently with the elastic data. Extracted octupole deformation parameters agree with those found in previous neutron analyses. The DWBA appears to give a good description of the inelastic angular distributions except for forward angles at 20.0 and 22.0 MeV. The present results do not exclude either energy- or isospin-dependent octupole deformations for ^{208}Pb. A careful, isospin consistent analysis of all nucleon inelastic scattering to this state would be necessary before more definitive conclusions could be justified.

In conclusion, the more precise, extended data base and improved search-code techniques have yielded a potential model which describes well neutron cross sections from 7 to 50 MeV incident energy. It represents a considerable improvement in terms of quality of fit and energy range covered over the previous work of ref. [3]. New insight into the general features and limitations of the optical potential has been gained.

The authors would like to extend their thanks to Dave Sturbois and Don Carter, whose technical expertise proved invaluable in running the experiment. The excellent cooperation of the computer services personnel at Ohio University and at Lawrence Livermore National Laboratory is gratefully acknowledged. Special thanks are also extended to R.P. DeVito and S.M. Austin for making available the neutron scattering data at 30 and 40 MeV. This work was supported by the National Science Foundation under grant number PHY-8108456 and by the U.S. Department of Energy under contract number W-7405-ENG-48.

REFERENCE

1. J. Rapaport, V. Kulkarni and R.W. Finlay, Nucl. Phys. A330, 15 (1979).
2. F.D. Becchetti and G.W. Greenlees, Phys. Rev. 182, 1190 (1969).
3. J. Rapaport, T.S. Cheema, D.E. Baimum, R.W. Finlay and J.D. Carlson, Nucl. Phys. A296, 95 (1978).
4. T.S. Cheema, Ph.D. dissertation, Ohio University, 1976 (unpublished).
5. D.E. Baimum, R.W. Finlay, J. Rapaport, J.D. Carlson and W.G. Love, Phys. Rev. C16, 1377 (1977).
6. W.T.H. Van Oers, Phys. Rev. C10, 307 (1974).
7. W.E. Kinney and F.G. Perey, ORNL-4909, 31 (1974).
8. G. Haouat, private communication (1981).
9. R. DeVito, Ph.D. dissertation, Michigan State University, 1979 (unpublished); R.P. DeVito, S.M. Austin, U.E.P. Berg and W. Sterrenburg, MSUCL-363 (1981).
10. R. De Leo and S. Micheletti, Phys. Lett. 98B, 233 (1981).
11. F.A. Brieva and J.R. Rook, Nucl. Phys. A291, 299, 317 (1977); A297, 206 (1978); A307, 493 (1978).
12. J.P. Jeukenne, A. Lejeune and C. Mahaux, Phys. Rev. C10, 1391 (1974); C15, 10 (1977); C16, 80 (1977).
13. F.S. Dietrich, R.W. Finlay, S. Mellema, G. Randers-Pehrson and F. Petrovich, Phys. Rev. Lett. 51, 1629 (1983).
14. R.K. Bhowmik, R.R. Doering, L.E. Young, S.M. Austin, A. Galonsky and S.D. Schery, Nucl. Instr. and Meth. 143, 63 (1977).
15. R. P. DeVito et al., Nucl. Instr. and Meth. 215, 423 (1983).
16. R. W. Finlay, C. E. Brient, D. E. Carter, A. Marcinkowski, S. Mellema, G. Randers-Pehrson and J. Rapaport, Nucl. Instr. and Meth. 198, 197 (1982) 197.

16. D.E. Carter, Nucl. Instr. and Meth. 160, 165 (1979).

17. W.E. Kinney, ORNL-TM-2052, Oak Ridge National Laboratory (1968).

18. J.R.M. Annand, Optical/Statistical Model Search Code, OPSTAT, Ohio University, 1983 (unpublished).

19. P.A. Moldauer, Nucl. Phys. A334, 185 (1980).

20. J.R.M. Annand and R.W. Finlay, Bull. Amer. Phys. Soc. 28, 737 (1983) and to be published.

21. P.W. Lisowski, G.F. Auchampaugh, M.S. Moore, G.L. Morgan and R.E. Shamu, Proc. Symp. on Neutron Cross Sections from 10-50 MeV, M.R. Bhat and S. Pearlstein, eds., BNL-NCS-51245, 301 (1980).

22. D.G. Foster and D.W. Glasgow, Phys. Rev. C3, 576 (1971).

23. G.C. Wick, Atti R. Accad. Ital. Memorie 13, 1203 (1943).

24. G. Bulski, W. Grum, J.W. Hammer, H. Postner, G. Schleussner and E. Speller, Proc. Int. Conf. on Nuclear Data, K. Bochoff, ed., Antwerp (1982).

25. J.P. Delaroche, C.E. Floyd, P.P. Guss, R.C. Byrd, K. Murphy, G. Tungate and R.L. Walter, Phys. Rev. C28, 1410 (1983).

26. C.D. Zafiratos, T.A. Oliphant, J.S. Levin and L. Cranberg, Phys. Rev. Lett. 14, 913 (1965).

27. I. Ahmad and W. Haider, J. Phys. G., Vol. 2, No. 9, 157 (1976).

28. P.D. Kunz, University of Colorado (unpublished).

29. J. Raynal (unpublished).

30. S.A. Fulling and G.R. Satchler, Nucl. Phys. A111, 81 (1968).

31. W.T. Wagner, G.M. Crawley, G.R. Hammerstein and H. McManus, Phys. Rev. C12, 757 (1975).

32. S. Mellema, Ph.D. dissertation, Ohio University, 1983 (unpublished).

33. F. Petrovich, private communication.

Table 1: Extrapolated forward angle cross sections, total elastic and reaction cross section from Legendre analysis of elastic scattering (cross sections in barns).

E(MeV)	L_{max}	$\frac{d\sigma}{d\Omega}(0°)\ \frac{b}{sr}$ [a]	σ_{total} [b]	σ_{Wick} [c]	$\sigma_{elastic}$ [d]	$\sigma_{reaction}$ [e]
7.0	13	7.11 ± 0.15	5.78 ± 0.06	7.07 ± 0.15	3.39 ± 0.07	2.39 ± 0.09
20.0	19	20.71 ± 0.62	5.85 ± 0.09	20.7 ± 0.62	3.33 ± 0.10	2.52 ± 0.13
22.0	20	22.91 ± 0.69	5.79 ± 0.09	22.3 ± 0.67	3.30 ± 0.10	2.49 ± 0.13
24.0	21	23.70 ± 0.71	5.67 ± 0.09	23.3 ± 0.67	3.22 ± 0.10	2.45 ± 0.13

a) $\frac{d\sigma}{d\Omega}(0°) = \sum_{L=0}^{L_{max}} a_L$. The a_L are determined in a least squares fit of the angular distrubution.

The quoted uncertainties are taken to be 2% at 7 MeV and 3% at 20 MeV and above and are almost entirely due to normalization uncertainty.

b) Refs. 21, 22; the data at 7 MeV from Ref. 22 have been averaged over an appropriate energy interval.

c) Wick's limit, using experimental σ_{total}, and $k = 0.2186\ \sqrt{E_{lab}\ (MeV)}\ fm^{-1}$

d) $\sigma_{elastic} = 4\pi a_0$, where a_0 is defined in a).

e) $\sigma_{reaction} = \sigma_{total} - \sigma_{elastic}$.

Table 2: Optical model parameters for ^{208}Pb+n obtained from 6 and 7 parameter individual best fits to the data. (Energies in MeV; lengths in fm) [a)]

	E_n	7.0	7.75*	9.0	10.0*	11.0	20.0	22.0	24.0	25.7	30.0	40.0
Real	V_r	44.56	46.22	45.18	44.73	44.30	44.71	45.69	45.08	41.23	42.95	42.14
	r_r	1.254	1.214	1.221	1.267	1.224	1.197	1.175	1.174	1.221	1.180	1.136
	a_r	0.659	0.6951	0.708	0.677	0.711	0.708	0.696	0.688	0.663	0.705	0.755
	J_V/A	399.9	378.3	377.4	411.6	372.8	352.4	341.6	335.3	334.7	325.1	290.9
	$\langle r_r^2 \rangle^{\frac{1}{2}}$	6.333	6.141	6.191	6.336	6.208	6.089	5.983	5.965	6.120	6.014	5.920
Imaginary	W_V	0.0	0.0	0.0	0.0	0.0	1.444	2.310	2.458	2.100	3.437	5.186
	W_S	6.740	7.018	6.347	7.913	5.588	5.719	4.109	3.604	5.712	3.796	-0.384
	r_i	1.310	1.249	1.301	1.302	1.278	1.195	1.255	1.289	1.198	1.255	1.514
	a_i	0.406	0.440	0.501	0.393	0.623	0.628	0.645	0.619	0.594	0.699	0.552
	J_W/A	41.27	40.15	46.30	45.14	49.49	55.72	56.84	55.59	59.29	67.43	74.01
	$\langle r_i^2 \rangle^{\frac{1}{2}}$	7.975	7.612	7.973	7.877	7.978	7.236	7.329	7.371	7.100	7.249	7.115
	χ^2/N	6.39	7.69	2.71	5.56	2.62	8.02	6.95	3.03	5.49	4.83	5.19

a) The following parameters were kept fixed during the search: $V_{S.O.} = 6.2$ MeV, $r_{S.O.} = 1.01$ fm, $a_{S.O.} = 0.75$ fm.

* Analyzing Power

Table 3: Common geometry optical potential, with volume real component only, for ^{208}Pb. (Energies in MeV; lengths in fm)

$V_V = 49.13 - 0.31\ E$ $\quad \lambda_D = 0.00$ $\quad V_{SO} = 5.75$ $\quad E < 50.0$

$r_R = 1.205$ $\quad r_{SO} = 1.105$

$a_R = 0.685$ $\quad a_{SO} = 0.499$

$\chi^2/N = 15.7$ [a)]

$W_V = -2.03 + 0.18\ E$ $\quad E > 11.20$ $\quad W_D = 6.36 - 0.47\ [10.71 - E]$ $\quad 7.0 \leq E \leq 10.71$

$= 6.36 - 0.13\ [E - 10.71]$ $\quad 10.71 < E < 50.0$

$r_I = 1.283$

$a_I = 0.569$

a) χ^2/N was calculated using the quoted uncertainties in differential cross sections and analyzing powers, and artificially low uncertainties ($\sim$ 0.1%) for the total cross sections.

Table 4: Common geometry optical potential, with volume and surface real components, for ^{208}Pb. (Energies in MeV; lengths in fm)

$V_V = 48.20 - 0.25\ E$ $\quad \lambda_D = 0.24$ * $\quad V_{SO} = 5.46$ $\quad E < 50.0$

$r_R = 1.198$ $\quad r_{SO} = 1.119$

$a_R = 0.708$ $\quad a_{SO} = 0.500$

$\chi^2/N = 12.2$ [a)]

$W_V = -2.37 + 0.20\ E$ $\quad E > 11.97$ $\quad W_S = 6.70 - 0.48\ (10.34 - E)$ $\quad 7.0 \leq E \leq 10.34$

$= 6.70 - 0.14\ (E - 10.34)$ $\quad 10.34 < E < 50.0$

$r_I = 1.291$

$a_I = 0.536$

* The real surface potential is parameterized as $\lambda_D V_D(r,E)$ where V_D is taken from Ahmad and Haider.[27)]

a) χ^2/N was calculated using the quoted uncertainties in differential cross sections and analyzing powers, and artifically low uncertainties ($\sim$ 0.1%) for the total cross sections.

Table 5: Octupole deformation parameters for the first 3^- state of ^{208}Pb.

Energy (MeV)	r_R (fm)	β_3	Deformation Length ($R_R \cdot \beta_3$)
7.0	1.202	0.137 ± 0.009	0.976 ± 0.064
20.0	1.202	0.123 ± 0.010	0.876 ± 0.070
22.0	1.202	0.124 ± 0.010	0.883 ± 0.070

FIGURE CAPTIONS

Figure 1 Background subtracted neutron time-of-flight spectrum for incident energy 22.0 MeV and 112° scattering angle.

Figure 2 Fitting a Legendre polynomial expansion to the 22.0 MeV differential elastic cross section. The integrated elastic cross section, extrapolated zero degree cross section, and χ^2 per degree of freedom plotted against the number of polynomials used.

Figure 3 Optical model fits, varying potential well depths only, to 7.0 and 22.0 MeV differential cross sections. Dashed lines denote fits made with the "optimum" 7.0 MeV geometry: r_R = 1.254 fm, a_R = 0.659 fm, r_I = 1.310 fm, a_I = 0.406 fm; solid lines for the optimum 22.0 MeV geometry: r_R = 1.176 fm, a_R = 0.696 fm, r_I = 1.255 fm, a_I = 0.645 fm.

Figure 4 The energy dependence of potential well depths using the common geometry of Table 3. Searching well depths but keeping the fixed common geometry produces the values shown as data points. ⊙--Real Woods Saxon;⊟--Imaginary Woods Saxon; ◇ --Imaginary Derivative Woods Saxon.

Figure 5 Differential cross sections fits using the constant geometry potential (Table 3). Data are from the following sources: 7.0, 20.0 22,0 and 26.0 MeV--present measurement; 9,0, 11.0 and 25.7 MeV--Rapaport et al.[3]; 30.0 and 40.0 MeV--DeVito et al.[9]

Figure 6 Analyzing power fits using the constant geometry potential of Table 3. The 7.75 MeV data are by Bulski et al.[24] and the 10.0 MeV data are by Delaroche et al.[25]

Figure 7 Constant geometry potential (Table 3) fit to the ^{208}Pb+n total cross section energy dependence. Data are from the following sources: ⊙ --Foster and Glasgow[22]; □ --Lisowski et al.[21]

Figure 8 Energy dependence of J_V/A and J_W/A (dashed line) for the present phenomenological potential (Table 3) compared with that calculated using the methods of Brieva and Rook[11] (points) ⊙ --real, □ --imaginary.

Figure 9 Inelastic cross sections for scattering to the 3^- state at 2.61 MeV for incident energies 7.0, 20.0 and 22.0 MeV. Solid lines denote DWBA fits.

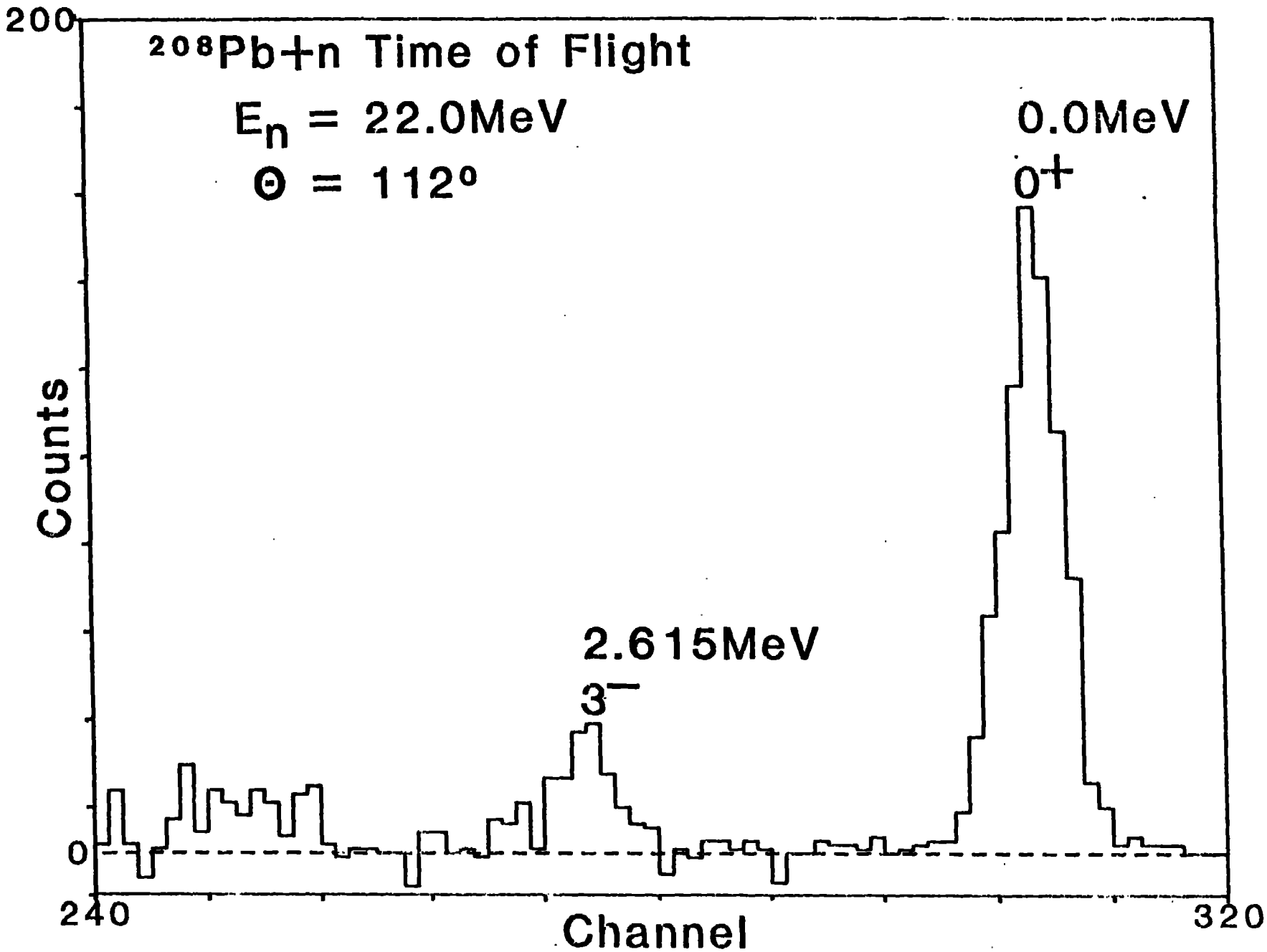
200
208Pb+n Time of Flight
En = 22.0MeV
Θ = 112°
0.0MeV
0+
Counts
2.615MeV
3−
0
240
Channel
320

Figure 1

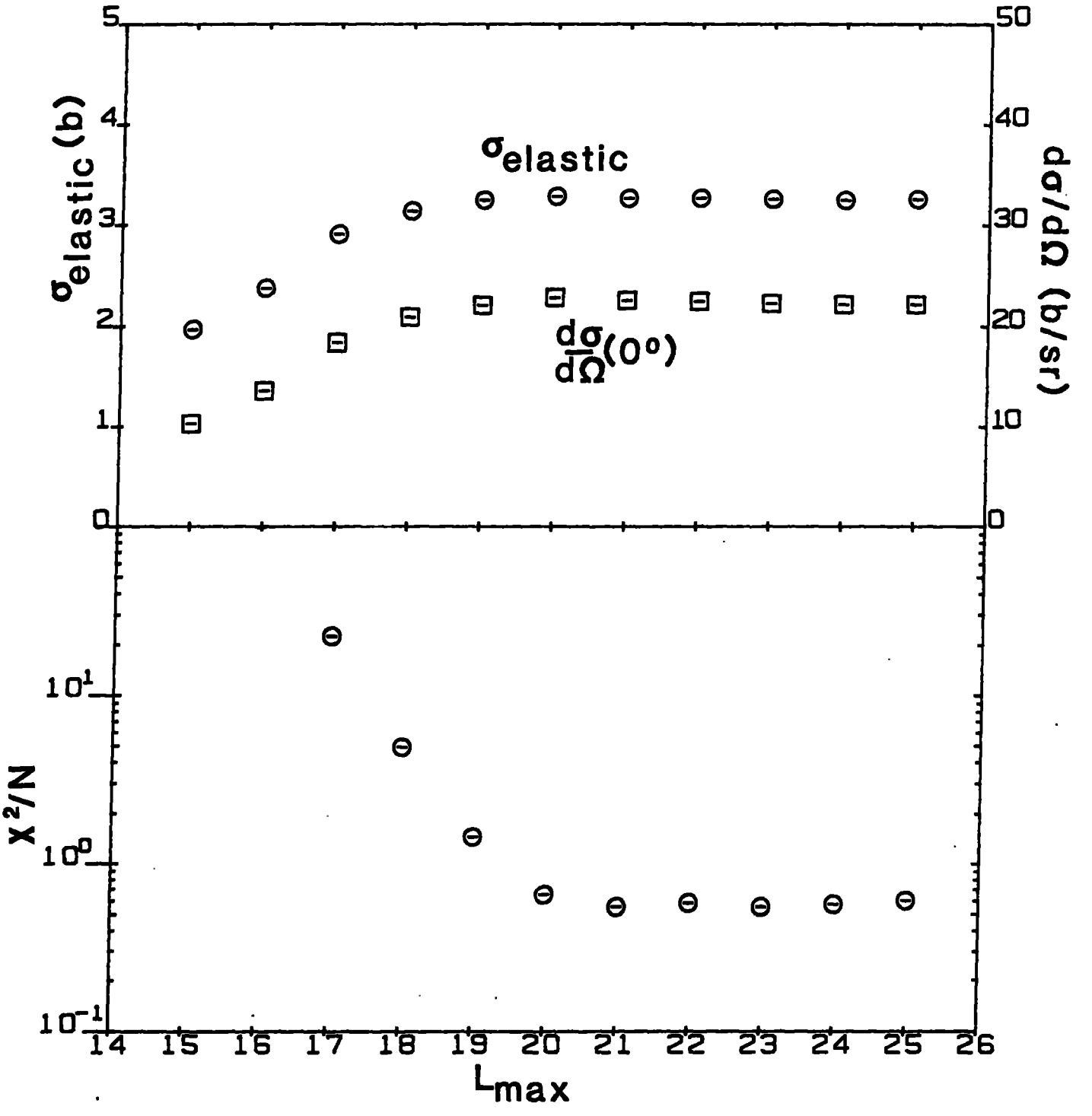

FIGURE 2

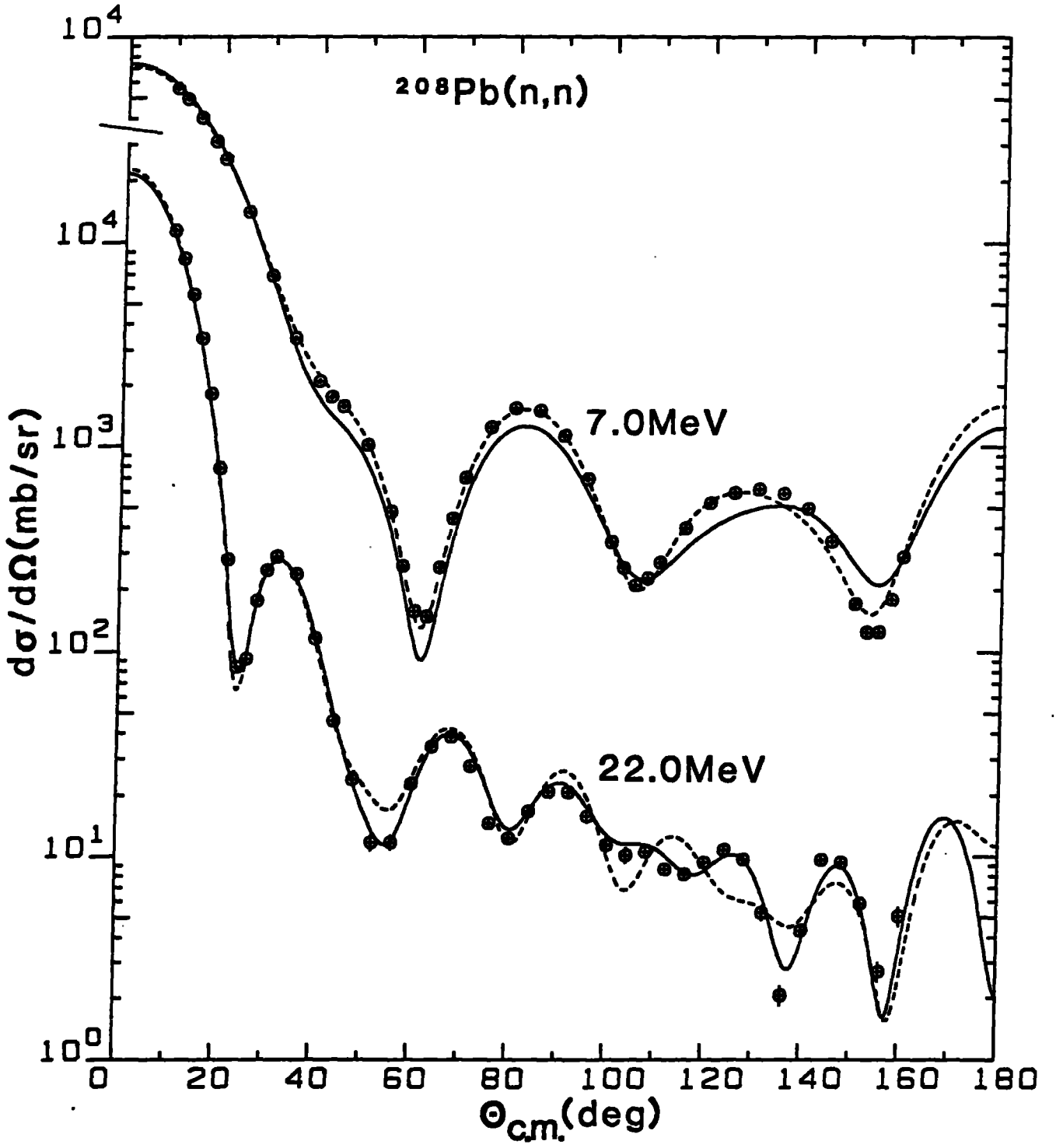
^{208}Pb(n,n)
7.0MeV
22.0MeV
dσ/dΩ(mb/sr)
$\Theta_{c.m.}$(deg)
10^4
10^3
10^2
10^1
10^0
0
20
40
60
80
100
120
140
160
180

FIGURE 3

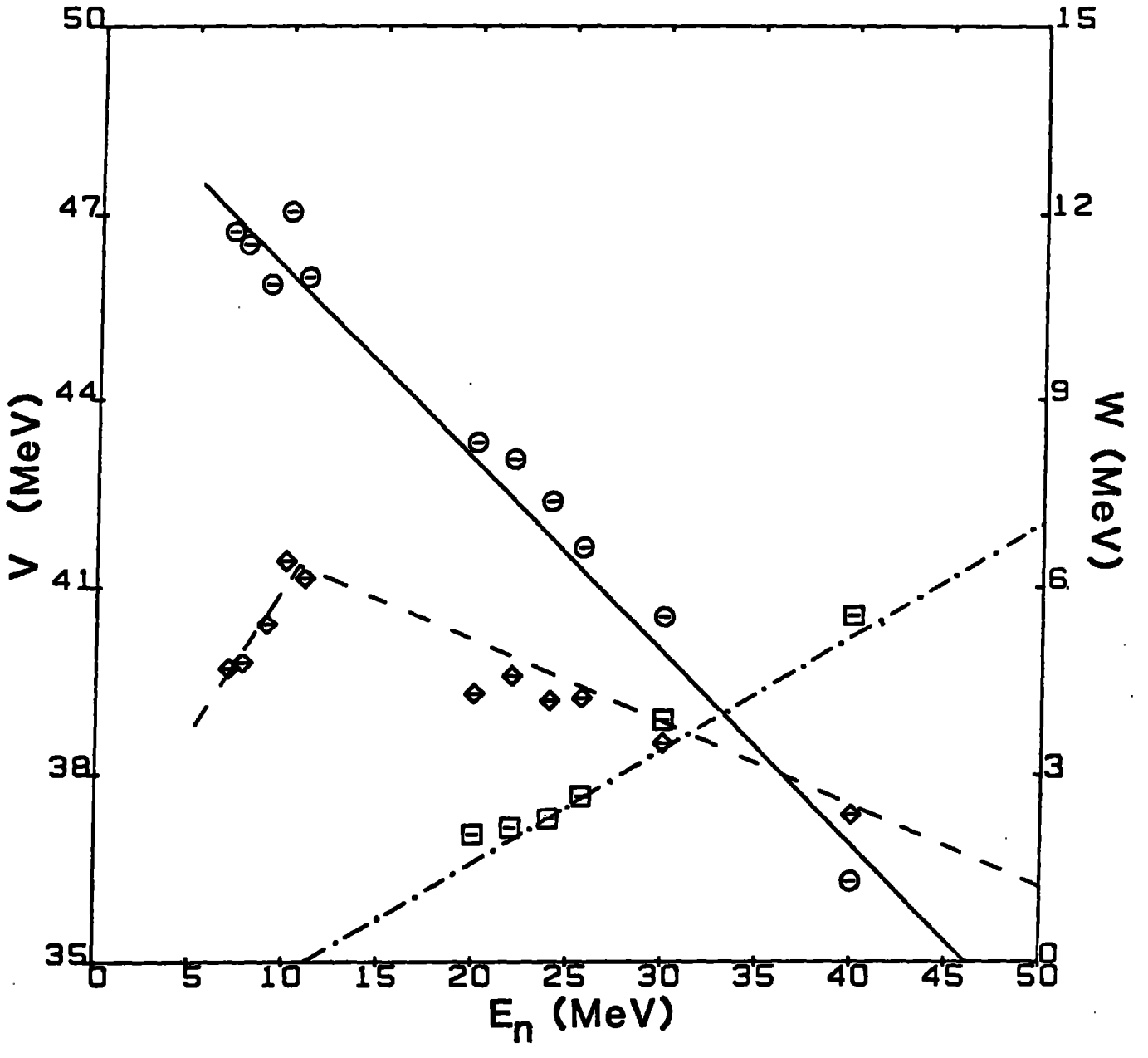
50
47
44
41
38
35
V (MeV)
15
12
9
6
3
0
W (MeV)
0
5
10
15
20
25
30
35
40
45
50
E_n (MeV)

FIGURE 4

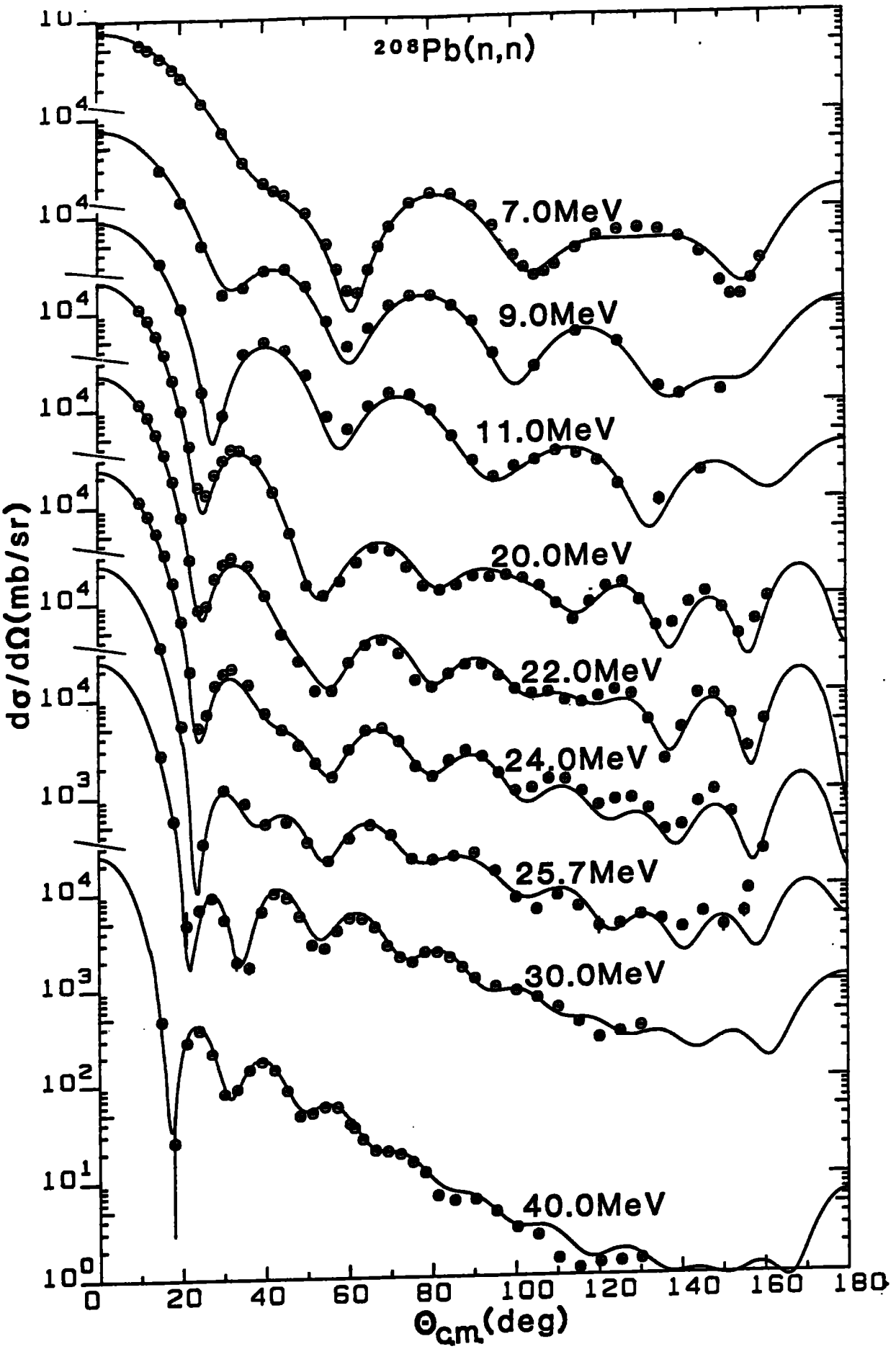
208Pb(n,n)
7.0MeV
9.0MeV
11.0MeV
20.0MeV
22.0MeV
24.0MeV
25.7MeV
30.0MeV
40.0MeV
dσ/dΩ(mb/sr)
Θcm(deg)
0
20
40
60
80
100
120
140
160
180

FI 5

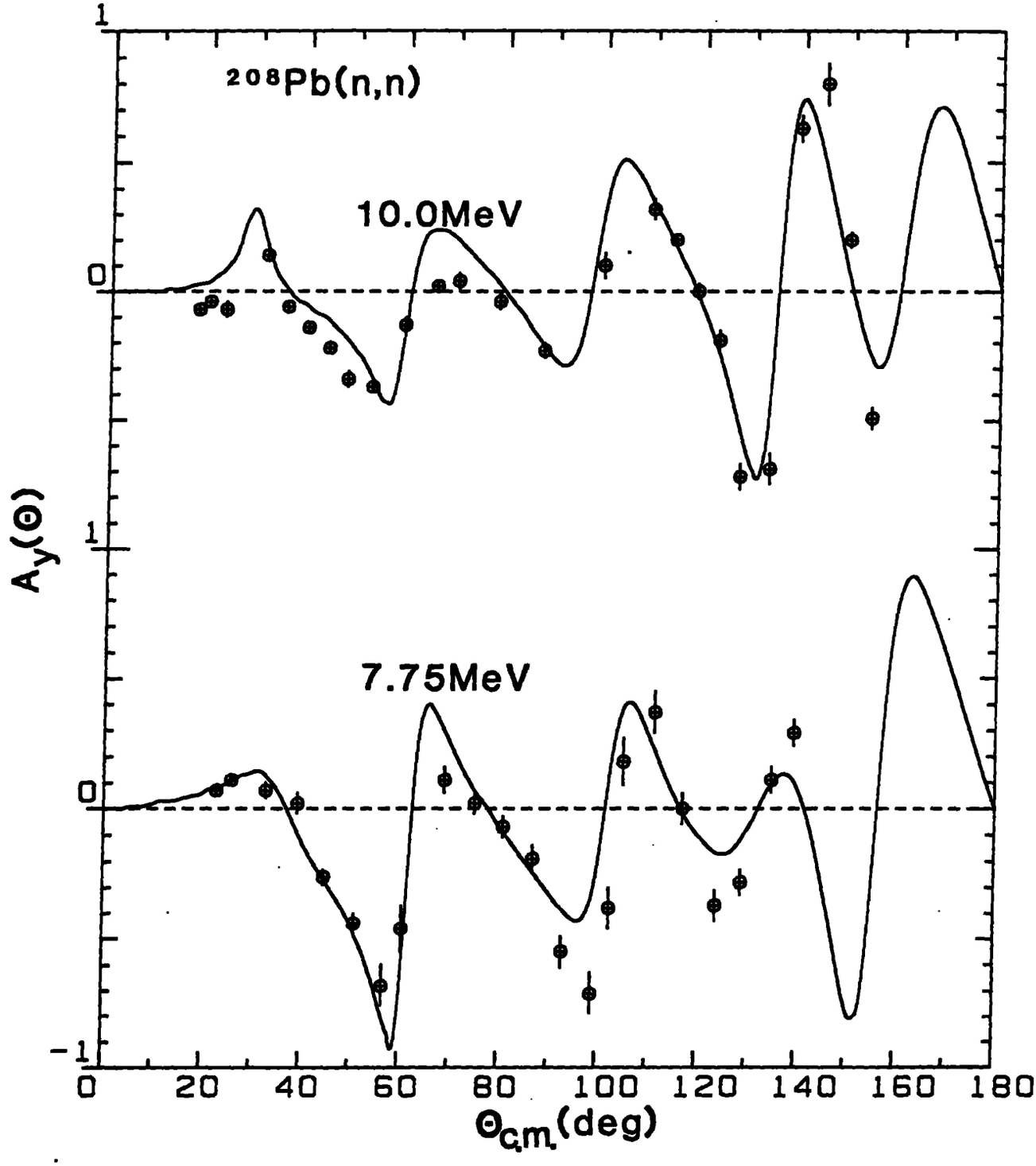
^{208}Pb(n,n)
10.0MeV
7.75MeV
$A_y(\Theta)$
$\Theta_{c.m.}$(deg)
1
0
-1
0
20
40
60
80
100
120
140
160
180

FIGURE 6

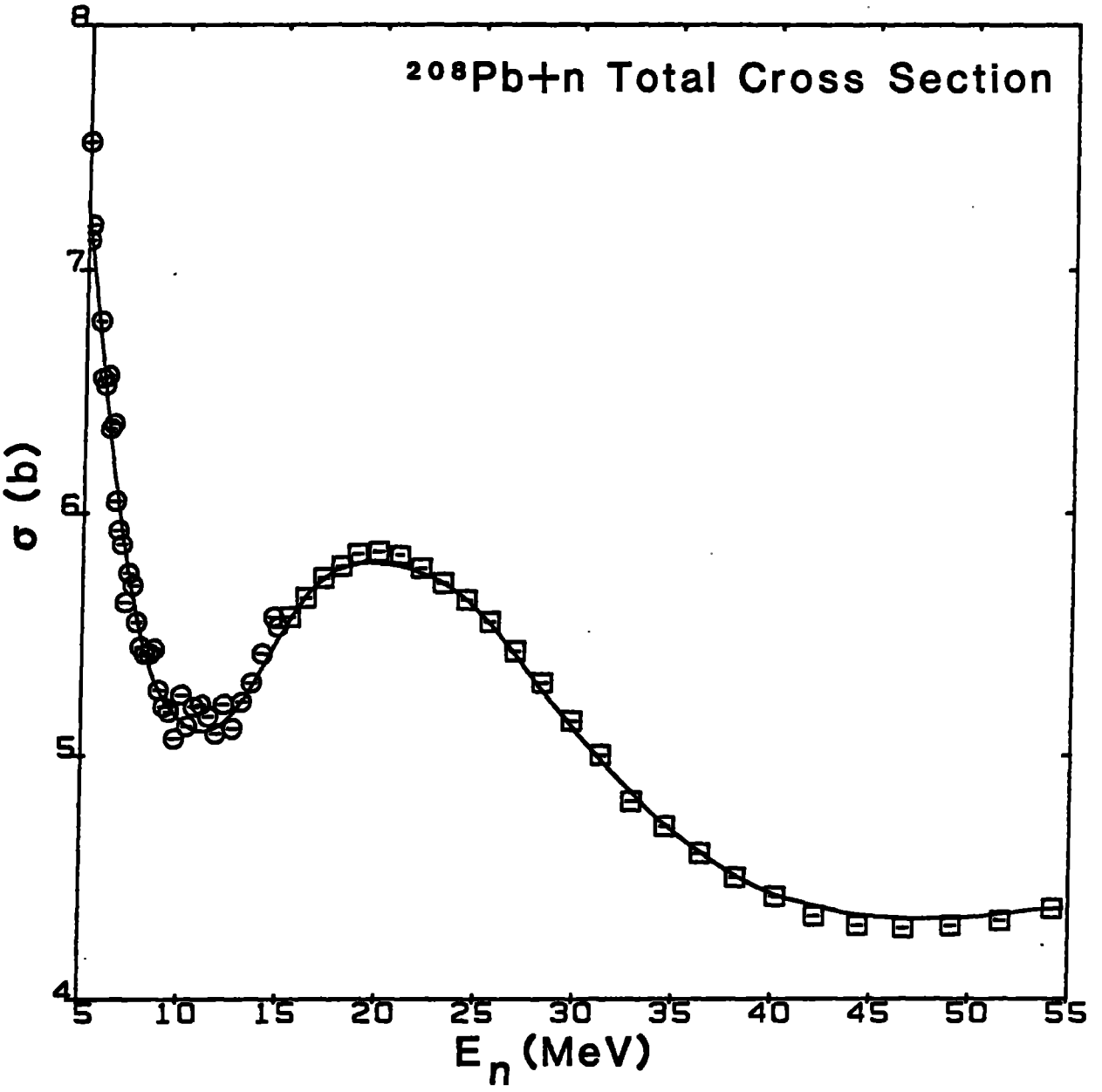
^{208}Pb+n Total Cross Section
σ (b)
8
7
6
5
4
5
10
15
20
25
30
35
40
45
50
55
E_n (MeV)

FIGURE 7

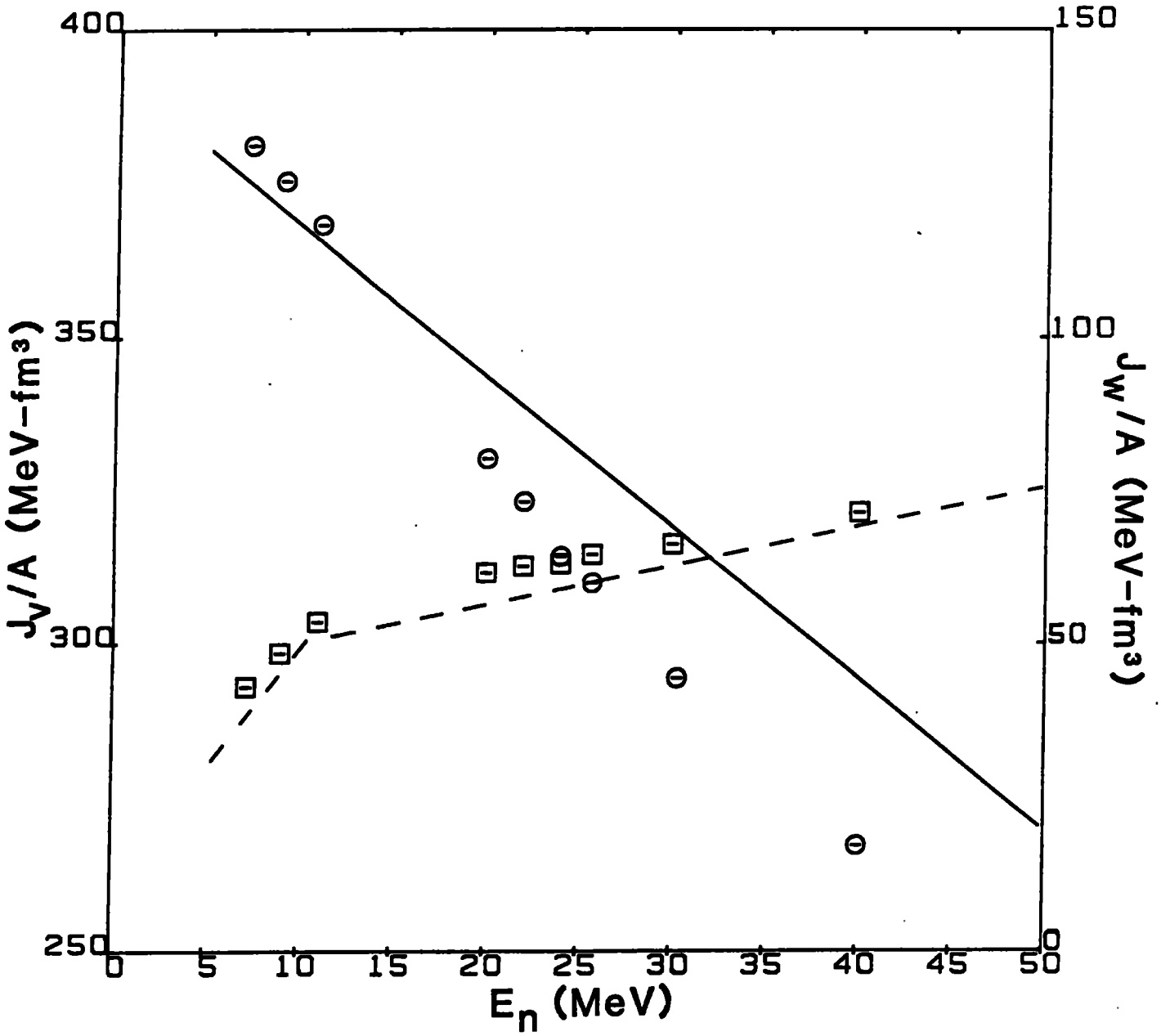
400
350
300
250
150
100
50
0
0
5
10
15
20
25
30
35
40
45
50
J_V/A (MeV-fm³)
J_W/A (MeV-fm³)
E_n (MeV)

FIGURE 8

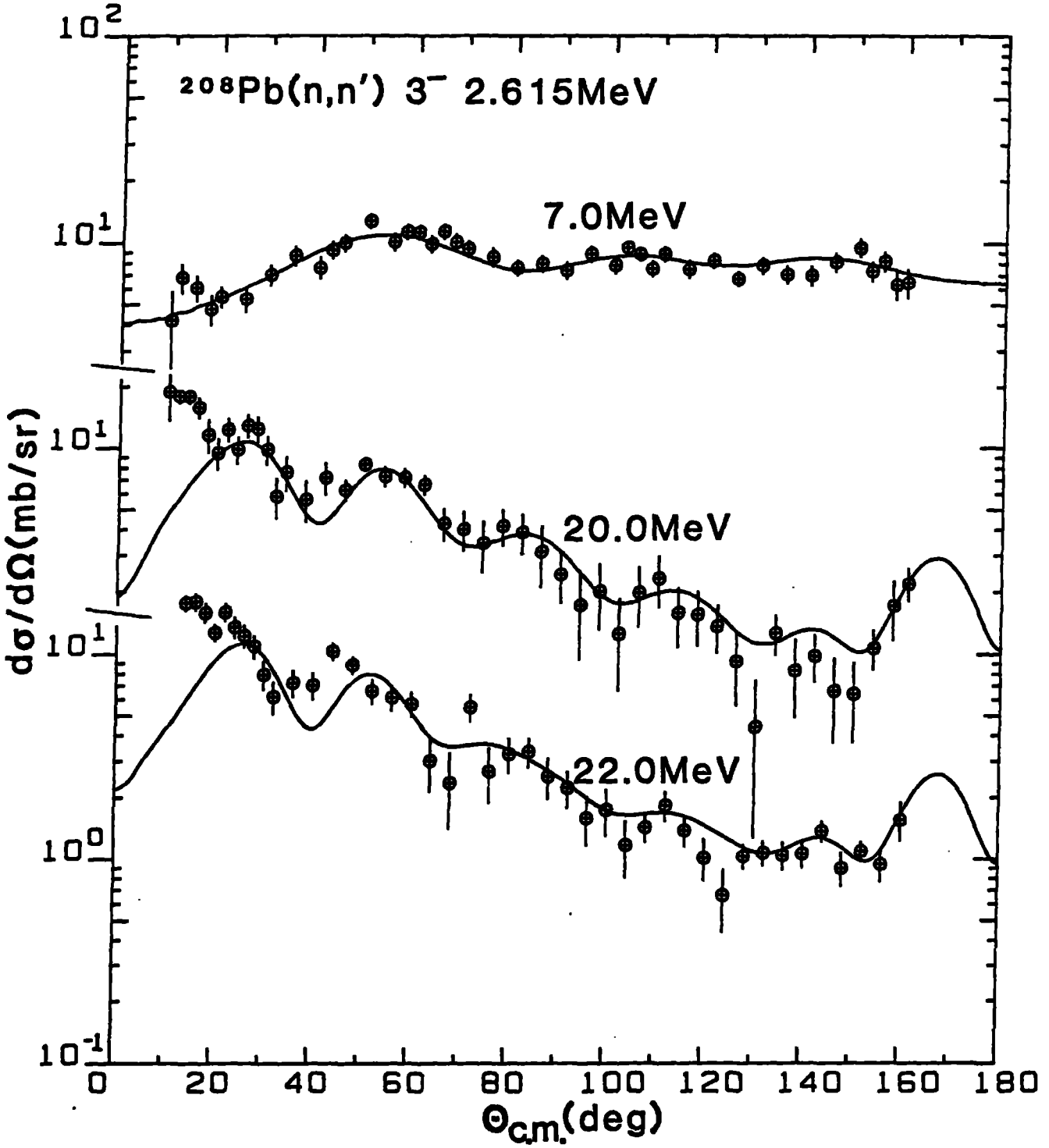
^{208}Pb(n,n') 3$^-$ 2.615MeV
7.0MeV
20.0MeV
22.0MeV
dσ/dΩ(mb/sr)
Θc.m.(deg)
10^2
10^1
10^1
10^1
10^0
10^-1
0
20
40
60
80
100
120
140
160
180

FIGURE 9